High resolution cryo-EM and crystallographic snapshots of the large actinobacterial 2-oxoglutarate dehydrogenase: an all-in-one fusion with unique properties

Lu Yang[1,2], Tristan Wagner[1§], Ariel Mechaly[3], Alexandra Boyko[1§], Eduardo M. Bruch[1§], Daniela Megrian[1], Francesca Gubellini[1], Pedro M. Alzari[1], Marco Bellinzoni[1]*

1. Institut Pasteur, Université Paris Cité, CNRS UMR3528, Unité de Microbiologie Structurale, F-75015 Paris, France
2. Wuhan Institute of Biological Products Co. Ltd., 430207 Wuhan, People's Republic of China
3. Institut Pasteur, Université Paris Cité, Plateforme de Cristallographie, F-75015 Paris, France

***Correspondence:** marco.bellinzoni@pasteur.fr

§Present addresses: T.W.: Microbial Metabolism Group, Max Planck Institute for Marine Microbiology, D-28359 Bremen, Germany; E.M.B: Sanofi, In vitro Biology, Integrated Drug Discovery, 350 Water St, Cambridge, MA 02141, USA

Abstract

Actinobacteria possess unique ways to regulate the oxoglutarate node located in the central position of the tricarboxylic acid cycle, a crossroad between energy conservation and nitrogen metabolism. Here, we studied the decarboxylative oxidation route that leads, through the 2-oxoglutarate dehydrogenase (ODH) complex, to the generation of succinyl-CoA and reduced equivalents to feed the respiratory chain. Compared to most organisms in which the oxidative decarboxylation and reductive acylation steps are carried out by different enzymes within the ODH complex, actinobacteria rely on an all-in-one protein (OdhA) in which both activities are carried out by the same polypeptide. We describe high-resolution cryo-EM and X-ray crystallography snapshots of representative enzymes from *Mycobacterium smegmatis* and *Corynebacterium glutamicum*, showing that OdhA is an 800-kDa homohexamer that folds into a three-blade propeller shape. The obligate trimeric and dimeric states of the acyltransferase and dehydrogenase domains, respectively, are critical for maintaining the overall assembly, where both domains interact via subtle readjustments of their interfaces. Complexes obtained with substrate analogues, reaction products and allosteric regulators illustrate how these domains operate. Furthermore, we provide additional insights into the phosphorylation-dependent regulation of this enzymatic machinery by the FHA (Fork-Head Associated) signalling protein OdhI, delivering new molecular details on how this actinobacterial-specific switching mechanism operates. Overall, the quaternary organization of OdhA represents a new piece of the fascinating puzzle of the synergistic, mixed pyruvate dehydrogenase/2-oxoglutarate dehydrogenase actinobacterial supercomplex.

Introduction

Acyl-CoA esters are the major metabolic carriers of carbon units in living organisms. The most conserved ways to their synthesis include the oxidative decarboxylation of 2-oxoacids carried out by three distinct dehydrogenase complexes: the pyruvate dehydrogenase complex (PDH) that feeds acetyl-CoA units into the TCA cycle, the branched-chain ketoacid dehydrogenase complex (BCKDH) involved in the catabolism of hydrophobic amino acids, and the 2-oxoglutarate dehydrogenase complex (ODH), which catalyses the synthesis of succinyl-CoA within the TCA cycle [1]. These enzymatic machineries are made by multiple copies of three enzyme components: the E1 component catalyses the thiamine diphosphate (ThDP)-dependent decarboxylation of the 2-oxoacid and its transfer to a lipoyl-lysine group, E2 transfers this acyl-moiety to the CoASH acceptor to generate acyl-CoA, and E3 is a FAD-dependent dehydrogenase that uses NAD^+ to oxidize the dihydrolipoyl moiety [2]. One or more lipoyl domains, which shuttle the reaction intermediate between the E1 and E2 active sites, are connected to the E2 catalytic domain through flexible linkers acting as swinging arms [1].

These ubiquitous complexes among aerobic organisms have long been thought to share a universally conserved architecture, characterized by a large hollow central core composed of multiple copies of the E2 catalytic domain, with a symmetry depending on the complex and the species [1,3]. The highly symmetric nature of the E2 core was first described by pioneer electron microscopy and X-ray crystallography studies [4,5], and largely confirmed afterwards [6–9]. The two other complex components, *i.e.* E1 and E3, are tethered to the core through the protruding E2 swinging arms [10,11], although determination of the stoichiometry and the molecular details of such interactions have long remained elusive. Very recently, single particle cryo-EM studies have shed light on substrate channelling in *E. coli* PDH [12], the most studied model for 2-oxoacid dehydrogenase complexes, as well as on the role of the E3 binding protein (E3BP) that is also part of the inner core in eukaryotic PDH complexes [13,14].

These highly conserved principles of 2-oxoacid dehydrogenase assembly, however, are not followed in Actinobacteria, one of the largest bacteria phyla. Earlier work had shown that *Corynebacterium glutamicum*, a well-known actinobacterial model largely used for biotechnological applications, possesses an enzyme, called OdhA, which bears succinyltransferase (E2o) and 2-oxoglutarate

decarboxylase (E1o) domains on the same polypeptide [15–17], a feature shared by the mycobacterial homologue KGD[18]. Considering the presence of such an 'all-in-one' fusion enzyme, which depends on lipoyl-lysine provided *in trans* as an acyl group carrier, and that DlaT (E2p) was reported to be the only lipoylated protein in mycobacteria [19], it was proposed that PDH and ODH may form a mixed supercomplex in those species, a hypothesis corroborated by the copurification of OdhA with components of the PDH complex in *C. glutamicum* [17]. The three-dimensional architecture of OdhA has however remained unknown so far, raising questions not only on how domains characterized by different oligomeric states may be arranged in the same polypeptide, but also about the composition, the size and the assembly of such a mixed PDH/ODH supercomplex. In addition, challenging even further the current 'dogma' of the universal conservation of PDH and ODH complexes, we recently showed that AceF (E2p) in actinobacterial PDH is reduced to its minimally active trimeric unit, due to a three-residue insertion at its C-terminal end that hinders any trimer-trimer interaction [20]. We also proposed that the presence of the C-terminal insertion and that of an *odhA*-like gene are related and constitute a signature of the Actinobacteria class [20]. Here, we show by X-ray crystallography and high-resolution cryo-EM, that corynebacterial OdhA and its mycobacterial orthologue KGD are large (~ 0.8 MDa) homohexameric enzymes with an unprecedented molecular architecture, and discuss how intra and interdomain interactions may account for their unusual regulatory properties.

Results

Actinobacterial OdhA/KGD is an 800 kDa homohexamer with two distinct catalytic centres

Our previous work with an N-terminal truncated form of *Mycobacterium smegmatis* KGD (*Ms*KGD$_{\Delta 115}$ clone designed based on limited trypsin proteolysis of the full-length protein) revealed the structure of the active E1o homodimer, in which each protomer was tightly associated to a monomeric E2o-like domain [18]. Since the acyltransferase catalytic activity is located at the junction of two E2 protomers [21], the obtained structure cannot reflect an active E2o state, and we hypothesized that the N-terminal truncation may have interfered with the assembly of the obligate homotrimeric state of this domain. We therefore decided to produce in *E. coli* the full-length proteins KGD from *M. smegmatis* and OdhA from *C. glutamicum* for further studies. [16]Crystals were obtained for both proteins, but their X-ray diffraction

was too limited for structural characterization. Therefore, we first proceeded by co-crystallizing *Ms*KGD with the inhibitor GarA for further stabilization, and we solved the structure of the *Ms*KGD-GarA complex at 4.6 Å resolution using the previously published *Ms*KGD$_{\Delta 115}$ structure [18] as the search model (**Table 1**). *Ms*KGD presents an homohexameric assembly (**Fig. 1**), which can be described as a three-blade, triangular propeller shape, approximately 20 nm wide and 15 nm thick. The E1o dimers containing the Mg-ThDP compose the blades, with two central E2o trimers sitting respectively on either side of the blades plane. This oligomeric arrangement as a trimer of dimers allows the separate E1o and E2o domains to maintain their canonical oligomeric arrangements (*i.e.* E1o dimers and E2o trimers) as seen in other oxoacid dehydrogenases, with their functional catalytic centres at the respective oligomeric interfaces. The inhibitor GarA binds full-length KGD in the same way as previously described for the high-resolution structure of the GarA-*Ms*KGD$_{\Delta 360}$ complex [22] (**Suppl. Fig. 1**), and the KGD E1o domain is indeed held in the resting conformation, as a result of GarA binding [22]. Interestingly, the low-resolution crystal structure also shows clear electron density, in four out of the six protomers, for a short helical hairpin engaged in intermolecular interactions (**Fig. 1**), which could be attributed to the N-terminal helical segment [16,18]. These observations suggest that the N-terminal domain of *Ms*KGD and OdhA could be involved in protein-protein interactions with other components of the complex, as it was recently reported for human E1o [23].

In parallel, the characterization of recombinant C. *glutamicum* OdhA showed a specific decarboxylase activity of 110.3 ± 1.0 nmol/min/mg, consistently with previous reports [16], and a sedimentation coefficient of 16.8 S (**Suppl. Fig. 2**), suggesting a predominant homohexameric state in solution, at all the tested concentrations. Therefore, based on the *Ms*KGD structure and on secondary structure predictions, we produced a truncated version of OdhA deprived of the flexible N-terminal segment (OdhA$_{\Delta 97}$), which produced crystals diffracting up to 2.5 Å resolution (**Table 1**). OdhA presenting indeed the same homohexameric assembly as *Ms*KGD (**Fig. 2**), all further structural analyses in this work will be focused on the higher resolution OdhA model. The single protomer shows the presence of an N-terminal acyltransferase (E2o) domain, spanning from the construct N-terminus to residue Asn349, connected by an 17-residue linker to the C-terminal, ThDP-dependent oxoglutarate

dehydrogenase domain (E1o) (**Suppl. Fig. 3**). In turn, the latter is made by a small helical domain (residues Asp367-Thr448) followed by three consecutive α/β subdomains, characteristic of homodimeric transketolases (**Suppl. Fig. 3**). In addition, a ThDP-Mg^{2+} cofactor is bound at the E1o domain dimeric interface (**Fig. 2**), in an equivalent pose and active site environment as in the *M. smegmatis* E1o (*Ms*KGD$_{\Delta 360}$) high-resolution crystal structures [18,24]. On the other hand, the E2o N-terminal domain shows the known, compact triangular trimeric conformation of the chloramphenicol acetyltransferase (CAT) family, characterized by an N-terminal β-strand that protrudes to make a strand exchange (mixed β-sheet) with the neighbouring monomer (**Suppl. Fig. 4**). The absence of such β-strand and the following α-helix in the *Ms*KGD$_{\Delta 115}$ construct may therefore explain initial failures in observing a functional E2o assembly [18]. Furthermore, despite the overall conservation of the CAT fold, a notable difference between the OdhA succinyltransferase domain and other E2o domains resides in the β-harpin that normally lies close to the three-fold axis and is located on the inside surface of the cubic assembly, here replaced by a short α-helix (connected by flexible linkers) which makes both intra and interchain contacts with the neighbouring E1o domains (**Fig. 2**; **Suppl. Fig. 4**). Structural alignment of the OdhA and *Ms*KGD E2o domains with characterized acyltransferase domains from other E2 enzymes confirms that this structural feature arises from a sequence insertion (**Suppl. Fig. 5**), and suggest it to be a trait of OdhA-like enzymes, as an adaptation to E2o-E1o fusions. As a result of this hexameric arrangement, the E1o and E2o active sites are poised at approximately 60 Å one to the other, with the oxoacid substrate and the acceptor CoASH getting access to them from different sides of the propeller 'blade' (**Suppl. Fig. 6**). Consistently, electron density maps pointed to the presence of CoASH, which was added to the cocrystallization mixture, bound to all E2o acceptor sites (**Fig. 2**), with the adenosine moiety adopting an equivalent pose to previously reported complexes with E2 enzymes [20,21].

Further inspection of the electron density maps revealed the presence of another 3'-phosphonucleotide, bound to the E1o domain in a pocket that was previously identified as the allosteric acetyl-CoA site in mycobacterial KGD [18] (**Fig. 2**). We therefore modelled this ligand as acetyl-CoA, noting that supporting electron density for the pantothenate chain was also absent in *Ms*KGD when crystals were soaked with

millimolar concentrations of acetyl-CoA, in the absence of the 2-oxoglutarate substrate (pdb 2XTA; **Suppl. Fig. 7**) [18], suggesting a shared regulation mechanism between the two enzymes.

High-resolution cryo-EM studies of OdhA

To study the conformational changes triggered by substrates or allosteric regulators that might affect the domain reorganization, high-resolution single particle cryo-EM was employed for further structural characterization. After assessing the suitability of full-length OdhA samples for single particle analysis using negative staining EM (**Suppl. Fig. 8**), plunge-frozen samples were prepared at different protein concentrations in the presence of the oxoglutarate analogue succinyl phosphonate (SP), previously shown to stabilize KGD [25]. Single particle cryo-EM allowed us to get a first OdhA map at 3.4 Å resolution, following *ab initio* reconstruction and 3D refinement applying dihedral D3 symmetry. However, the narrow particle distribution precluded us to improve the map resolution. Raising OdhA concentration up to about 8 mg/ml and including 8 mM CHAPSO in the sample before plunge-freezing allowed a significant improvement of both the number of particles per micrograph and their orientation distribution (**Fig. 3a/b**), as reported in other cases [26], increasing the resolution of the reconstructed map up to 2.3 Å (**Suppl. Fig. 9**). A further improvement of the map up to 2.2 Å (Fig. 3c) was obtained by combining maps generated by local refinement of the two separate domains (**Suppl. Fig. 9**; **Suppl. Movie 1**). The same grid preparation strategy was then applied to other full-length OdhA samples, *i.e.* enzyme without added ligands, or preincubated with either CoASH or succinyl-CoA, leading to maps at comparable resolutions of 2.1-2.2 Å (**Table 2**). In all cases, the maps, which showed well-defined density for most side chains, allowed to trace the OdhA polypeptide chain unambiguously starting from residue Pro102, corresponding to the N-terminal boundary of the E2o domain, with excellent stereochemical parameters (**Table 2**). In contrast, the full N-terminal OdhA segment, corresponding to the first hundred residues that include a predicted helical hairpin analogous to the one observed in the crystal structure of *Ms*KGD (Fig. 1b), could not be traced due to the lack of supporting density, confirming its high mobility in solution. The E1o active site at the dimer interface showed a clear density for ThDP-Mg^{2+} in all cases (**Suppl. Fig. 10**). In the case of the OdhA-SP complex, the phosphonate molecule, determined by surface plamon resonance to bind OdhA with a K_D of 119 ± 17

μM, could be modelled as covalently linked to the reactive C2 carbon from the ThDP thiazolium ring (**Suppl. Fig. 11**). Such adduct, equivalent to the one generated upon cocrystallization of *Ms*KGD$_{\Delta 360}$ (PDB 6R29 [25]), provides an excellent mimic of the pre-decarboxylation complex and, in turn, of the incoming 2-oxoglutarate substrate (**Suppl. Fig. 11**).

Previous work on *Ms*KGD has shown the existence of two different conformational states of its E1o domain, *i.e.* a resting (or *early*) state *vs.* an activated (or *late*) state [18,24]. The activated state was trapped following the addition of substrates and was associated to post-decarboxylation ThDP-bound intermediates deriving from either 2-oxoglutarate or 2-oxoadipate [24], or phosphonate analogues [25]. In contrast to the crystallographic structure of OdhA$_{\Delta 97}$ which fits the resting state, all our models refined on single particle EM maps adopt an activated conformational state of the E1o domain, even in the absence of added ligands. The state is indeed revealed by the shifts in the loops 566-579 as well as 809-836, that could be traced in the EM structures but were mostly unstructured in the OdhA$_{\Delta 97}$ crystal structure (**Fig. 3d/e**; **Suppl. Fig. 12**) [18,24]. However, all the OdhA cryo-EM datasets, including those corresponding to complexes with CoASH, succinyl-CoA and SP, show an acetyl-CoA molecule bound to E1o allosteric site which could be positioned unambiguously (**Fig. 3d/e**; **Suppl. Fig. 13**). The presence of a bound acetyl-CoA activator, most likely acquired following heterologous overexpression of the enzyme in *E. coli*, may therefore explain the observed OdhA activated conformation through a mechanism that involves the stabilization of the loop 809-836 in its extended form (**Suppl. Fig. 13**), promoting, in turn, the activated conformation [18]. This hypothesis is supported by previous observations showing that acetyl-CoA binding to *Ms*KGD contributed to stabilize the activated conformation [18], as well as by steady-state kinetic and spectroscopy studies that concluded that acetyl-CoA acts as a mixed V and K type allosteric activator on mycobacterial KGD [27].

The ensemble of high-resolution OdhA single-particle cryo-EM complexes provides also novel insights into the functionality of the E2o succinyltransferase domain. First, the OdhA-CoASH complex shows the bound CoASH with the pantothenate chain not entering the active site, but with the terminal, reactive sulphydryl group accommodated in the mostly hydrophobic pocket defined by Leu200, Ala201, Thr258

and the side chains of Ile202 and Leu257 (**Fig. 4a**). Such CoASH binding mode is close to the previously reported 'out' conformation of CoASH in the non-proficient, ternary complex of *Azotobacter vinelandii* E2p (PDB 1EAB) (**Suppl. Fig. 14**), where it was proposed as a mechanism to protect the reactive sulfhydryl group from oxidation [21]. In contrast, succinyl-CoA binds to the same domain with its 2-phosphoadenosine moiety superimposable to the one observed for CoASH, but the pantetheine arm directed towards the E2o active site. Noteworthy, its pose is overall very close to the one shown by CoASH in its ternary complex with lipoamide in AceF (E2p) from *C. glutamicum* [20] (**Suppl. Fig. 15**). Specifically, the sulphur atom is positioned at 5 Å from the NE2 nitrogen of the catalytic His316 belonging to the neighbouring subunit (**Fig. 4b**), a distance compatible with the proposed catalytic mechanism [21], while the terminal carboxyl group from the succinyl moiety is stabilized by hydrogen bonds with Ser129 and Tyr314, also provided by the adjacent subunit. At the same time, the ketone oxygen acts as H-bond acceptor to Thr258 and Ser268 (**Fig. 4b**; **Suppl. Fig. 15**). The observed succinyl-CoA binding mode agrees with mutagenesis data pointing to a catalytic role for His316 and Gln320, and suggesting Thr258 as involved in CoA binding (**Suppl. Fig. 15**) [16]. It is worth to note that both Ser129 and Tyr314 are conserved among OdhA orthologues (**Suppl. Fig. 16**) as well as in structurally characterized E2o enzymes, but not in E2s with different substrate specificity (**Suppl. Fig. 5**), consistently with the observed role of these residues in stabilizing the terminal carboxyl group from the succinyl moiety. Our snapshots therefore suggest them as one of the structural features that may contribute to provide substrate selectivity to E2 enzymes.

FHA regulation: specific interactions for a conserved inhibition mechanism

By preincubating purified OdhA with an excess OdhI and passing the sample through size exclusion chromatography prior to grid preparation, we were also able to obtain a single particle reconstruction of a full OdhA-OdhI complex at 2.3 Å resolution (**Suppl. Movie 2**). The overall structure is very similar to that of the homologous *Ms*KGD-GarA complex (**Fig. 5a**), with OdhI molecules binding, through their FHA domains (traceable for residues Glu40-Ala142), to the OdhA E1o domain with a 1:1 stoichiometry. In contrast to the other single particle EM structures, OdhA adopts here the resting conformation, equivalent to the one observed in the crystal structure of $OdhA_{\Delta 97}$ and consistently with

structural and kinetic observations on mycobacterial KGD, both indicating that GarA binding stabilized this enzyme conformation [22,27]. Moreover, no ligand bound to the OdhA acetyl-CoA allosteric site could be detected in this complex, suggesting that bound acetyl-CoA may have been lost because of OdhI binding, further confirming the link between the presence of the activator and the conformal state of the enzyme.

Interactions with OdhA involve the tips of both OdhI FHA antiparallel β-sheets: one anchors firmly to the OdhA loop Leu591-Glu598, which connects two antiparallel β-strands, while the tip of the other OdhI β-sheets binds the OdhA α-helices Gln480-Lys503 and Asn786-Asn805 (αE) (**Fig. 5b**). The interactions of the former involve the OdhI positively charged Arg53, Lys132 and Arg134 side chains which bind, through a network of hydrogen bonds, to main chain carbonyl oxygens of the OdhA 591-598 loop, in a similar way as in the *Ms*KGD-GarA complex (**Fig. 5b**). However, the interactions between OdhI and the OdhA helix αE, which is a landmark of the enzyme activation state [18,24], show a few significant differences when compared to the mycobacterial complex. The αE helix could only be traced till residue 805 in OdhA, and it shows a 30° kink towards OdhI at its N-terminal tip (**Fig. 5c**). Most notably, no hydrogen bond was observed between the phosphomimetic residue Asp795 in OdhA and OdhI Ser86, in contrast to structural observations on the GarA-*Ms*KGD complex [22,28] but consistently with site-directed mutagenesis on OdhI, which pointed to Ser86 as dispensable for binding [29]. Accordingly, the binding affinity of the GarA S95A variant for *Ms*KGD was comparable to the wild-type [22].

A negatively charged side chain from Asp798, adjacent to Asp795 on the αE outside surface (instead of a glycine in *Ms*KGD and other orthologues; **Suppl. Fig. 16**), exists additionally in OdhI within hydrogen-bonding distance to the main chain amino group of Arg87. The side chain of the same Arg87, in turn, is involved in a salt bridge with OdhA Glu801 (**Fig. 5b/c**), pointing to a key role of this residue in the OdhI-OdhA interaction. In agreement with these observations, mutations leading to the substitution of OdhI Arg87 to either proline or alanine have been isolated in suppressor mutants of a *glnX* gene deletion in *C. glutamicum*, where the impaired OdhA inhibition overcomes the accumulation

of unphosphorylated OdhI [30]. In the same work, a missense mutation involving OdhI Leu107 was also isolated in a mutant strain bearing the same suppressor phenotype [30], consistently with this residue being located at the OdhA-OdhI interface. Leu107 is indeed involved in van der Waals interactions with OdhA Ala791 and the side chains of both Lys484 and Gln488 (**Fig. 5c**; **Suppl. Fig. 17**), the substitution of which was shown to impair the *Ms*KGD-GarA interaction [22]. Overall, the OdhI relative position is shifted approximately 2 Å aside from OdhA when compared to GarA in the corresponding mycobacterial *Ms*KGD-GarA complex (distance calculated as the RMSD over the ensemble of Cα; **Suppl. Fig. 17**), resulting in a ~ 5 Å distance between the OdhI Ser86 OG atom and the carboxyl group of OdhA Asp795. An additional, distinct intermolecular interaction in OdhA-OdhI is due to the presence of a serine residue at OdhA position 802, still positioned on the αE helix and making a hydrogen bond to OdhI Arg72 (**Fig. 5b**), while an arginine is found at the corresponding position in *Ms*KGD, as well as in other OdhA-like enzymes (**Suppl. Fig. 16**). Replacing this residue by an alanine was indeed found to decrease 6.25-fold the K_i of GarA for KGD [22]. Overall, despite a similar molecular surface occluded on the FHA domain upon the interaction with either *Ms*KGD or OdhA (around 950 Å^2), and a conserved inhibition mechanism, our high resolution cryo-EM model provides a molecular view to explain the 100-fold lower K_D of OdhI on OdhA [29] *vs*. GarA on *Ms*KGD, as determined by surface plasmon resonance [22].

Interactions between the two catalytic centres

The unprecedented homohexameric arrangement of OdhA challenges current paradigms about the composition and protein-protein interactions within PDH and ODH complexes, and raises new exciting questions on the coordination of the different catalytic activities carried out by the same polypeptide. We previously reported how the E2o domain contributes to regulate E1o activity in *Ms*KGD by restraining protein motions involved in the transition from the resting to the active state [18]. An arginine residue (Arg781) situated on the loop preceding the αE helix was indeed shown to mediate contacts with the E2 domain, and the analysis of available sequences of OdhA homologues from Actinobacteria shows the conservation of this residue (**Suppl. Fig. 16**). In the resting state OdhA$_{\Delta 97}$ crystal structure,

Arg781 hydrogen bonds to the main chain oxygens of Arg151 and Thr152, but these interactions are not observed in the EM models (including the OdhA-OdhI complex), where the distance of the guanidium group from the Arg151 carbonyl oxygen is around 7 Å. A salt bridge in between Asp777 (helix αE) and Arg153 from the E2o domain is observed instead (**Suppl. Fig. 18**). Intrigued by these differences that suggest interdomain mobility, we performed 3D variability analysis [31] on all our EM datasets. The results indicate indeed a twisting movement of the longitudinal axis of the E1o domain, which deviates from its average position on the three-fold axis of the hexamer, as well as tilting of the E1o domain on the hexamer plane (**Suppl. Movie 3**), reinforcing the hypothesis that interdomain flexibility is a major contributor to protein dynamics, which, by remodelling the contact network, may contribute to enzyme regulation.

The homohexameric OdhA architecture also provides a further example of conservation of structural motifs at the domain interfaces. We showed recently how actinobacterial E2p enzymes lose their typical high molecular weight oligomerization due to a specific 3-residue insertion at their C-terminus, and as a consequence they are reduced to their minimal catalytic homotrimeric state [20]. Specifically, the insertion makes the terminal 3_{10} helix, involved in symmetric trimer-trimer interactions, to deviate from its position making intramolecular contacts instead. It is worth to note that a similar situation is observed at the E2o-E1o interface in OdhA, where the C-terminal amphipathic α-helix from the E2o domain adopts a conformation substantially equivalent to the one observed in AceF (**Fig. 6a**), its internal face being held against helix α3 from the same domain (OdhA residues Phe159-Ala173), mostly by hydrophobic interactions. Moreover, a phenylalanine residue (Phe340 in OdhA) occupies a structurally equivalent position to Phe669 in AceF (**Fig. 6a**), shown to be a key conserved residue of the 3-amino acid insertion in actinobacterial E2. Likewise, as observed in AceF, the Phe340 OdhA side chain contributes directly to fill the hydrophobic pocket which, in canonical E2 enzymes, would accommodate the incoming C-terminal 3_{10} helix from the facing trimer, in the so-called 'knobs and socket' interaction. Consistently, sequence alignment of OdhA orthologues shows the conservation of the phenylalanine residue (**Fig 6b**; **Suppl. Fig. 16**), in agreement with previous considerations [20] and

thus confirming the role of the phenylalanine-containing insertion (PCI) as a structural motif in actinobacterial E2 enzymes.

Discussion

2-oxoacid dehydrogenase complexes have long made a textbook example of megadalton-sized, universally conserved multienzymatic machineries, each dedicated to specific, yet conserved, three-step reactions located at the core of central metabolism. These complexes have, so far, been thought to be centred around large hollow cores composed of multiple copies of specific E2 (acyltransferase) enzymes, which, through long and flexible linkers that bear lipoyl and interaction domains, anchor the E1 (ThDP-dependent decarboxylases) and E3 (lipoamide dehydrogenase) components on the outside surface. Despite the first evidence of such architecture dates back to pioneering investigations in the sixties [4,5], the inherent flexibility of the E2 interdomain linkers, and the transient nature of some of the protein-protein interactions has long hampered a detailed understanding of such complexes. Even their stoichiometry, including in well-studied model organisms like *E. coli*, has long been a matter of debate. Thanks to methodological advances in single particle EM, the last couple of years have however seen significant advances in the field, ranging from the composition of eukaryotic E2p and E2o cores [13,14,32–34], to snapshots of protein interactions and substrate channelling, leading to new insights into the transacylase reaction and the dihydrolipoamide access into the E2 active site [12,32]. None of the aforementioned studies, however, dealt with complexes deviating significantly from the well-established general architecture of oxoacid dehydrogenases. Here, by a combination of high-resolution X-ray crystallography and cutting-edge single particle EM analysis, we show for the first time how evolution, through shuffling and fusion of domains, combined fully functional E2o and E1o activities in a single polypeptide. Despite the presence of such domain fusion was first reported in the nineties [15], the three-dimensional organization of such a 0.8 MDa, ‘all-in-one’ enzyme had so far resisted attempts at structural charaterization. We also provide atomic-resolution details of bound cofactors, substrate analogues and products, and provide new insights into the allosteric regulation mechanism driven by an FHA module, another distinguished feature of Actinobacteria. The unique, homohexameric three-blade propeller shaped state of KGD and OdhA not only stands off for its size and symmetry, but sheds

a completely new light on the field, raising new questions about the evolution of PDH and ODH complexes. The coexistence of ThDP-dependent dehydrogenase and succinyltransferase domains on the same polypeptide, and their interactions, has obvious implications not only in terms of substrate channelling and catalytic efficiency, but also in terms of regulation, as first suggested by our previous studies on mycobacterial KGD [18]. Furthermore, here we show how the succinyltransferase domain makes use of the same C-terminal structural motif we previously identified in corynebacterial AceF, and adds to the hypothesis of a link between the presence of an OdhA-like, 'all-in-one' enzyme and a mixed PDH/ODH supercomplex, which presence, initially proposed on the basis of copurification experiments in *C. glutamicum* [17], has been supported by increasing experimental evidence [16,18,35]. It is therefore tempting to speculate that the correlation between the presence of an OdhA-like enzyme bearing both E2o and E1o activities, and a reduced E2p core may be related to the size and hexameric architecture of OdhA, possibly incompatible with its interaction with a canonical cubic or dodecahedral PDH core. How the same E2p lipoyl domains may be able to serve the catalytic sites of OdhA as well as those of E1p and E2p itself is indeed one of the most interesting open questions [36]. The reasons usually evoked as the major advantages brought in by the assembly of large, multimeric complexes, *i.e.* active site coupling and efficient substrate channelling, may actually turn out to be, as pointed out following the publication of our previous study, just 'one side of the coin' [36]. The physical proximity of the PDH and ODH centres is likely to facilitate the coregulation of the pyruvate and oxoglutarate nodes, as indicated by the positive regulation of both OdhA and *Ms*KGD by acetyl-CoA, which suggests the presence of positive feedback mechanisms. The next challenging goals will include determining how OdhA and the other components of the PDH/ODH supercomplex may be physically and temporally assembled in a supramolecular structure, and whether such an assembly could interact with other cellular structures. Nevertheless, new avenues are from now on open in the field, and will lead to a better understanding of fundamental biological processes like the regulation of central metabolism, as well as to novel therapeutic approaches that may target Actinobacteria-specific protein-protein interactions.

Acknowledgements

This work was funded by the ANR projects SUPERCPLX (ANR-13-JSV8-0003) and METACTINO (ANR-18-CE92-0003), both granted to M.B., and by institutional funds from the Institut Pasteur and the CNRS. We are grateful to the core facilities at the Institut Pasteur C2RT (Centre for Technological Resources and Research) and their respective staff, namely to A. Haouz, P. Weber and C. Pissis for performing crystallization screenings, B. Raynal, S. Brûlé and S. Hoos for their assistance in analytical ultracentrifugation and buffer optimization, P. England for his help with surface plasmon resonance experiments, J.-M. Winter, S. Tachon and M. Vos for assistance with EM data collection. We are also grateful to N. Barilone, I. Miras and P. Vilela for their initial work in plasmid generation and protein expression, and to A. Bezault, G. Péhau-Arnaudet and C. Rapisarda for their help in grid preparation and EM data collection. We acknowledge the synchrotron sources Soleil (Saint-Aubin, France), and ESRF (Grenoble, France) for granting access to their facilities, and their respective staff for helpful assistance, in particular E. Kandiah for performing EM data collection on CM01 (ESRF). The NanoImaging Core at Institut Pasteur was created with the help of a grant from the French Government's 'Investissements d'Avenir' program (EQUIPEX CACSICE, ANR-11-EQPX-0008), and is acknowledged for support with cryo-EM sample preparation, image acquisition and analysis. L.Y. and A.B. have both been affiliated to the Pasteur – Paris University (PPU) International PhD program; L.Y. was funded by the Wuhan Institute of Biological Products Co. Ltd. (Wuhan, People's Republic of China), subsidiary company of China National Biotec Group Company Limited, and by a doctoral fellowship from the China Scholarship Council (CSC). Succinyl phosphonate was a kind gift from V. Bunik (Lomonosov University, Moscow).

Author Contributions

L.Y., T.W. and A.B. produced and purified recombinant proteins; L.Y., T.W., A.B., F.G. and M.B. collected data; L.Y. prepared cryo-EM grids; L.Y. and A.M. analyzed cryo-EM data; L.Y., T.W., A.M. and M.B. refined models; L.Y. performed biophysical experiments; D.M. performed bioinformatic analysis; P.M.A. provided advice on data interpretation and contributed to the manuscript; M.B. supervised the work and wrote the paper. All authors reviewed the manuscript and agreed on its content.

Materials and Methods

Plasmid construction. Expression constructs pET-28a-TEV/OdhA and pET-28a-TEV/OdhI were generated by Genscript (Leiden, the Netherlands), providing a sequence coding for the TEV protease cleavage site (ENLYFQG) between the vector encoded His_6-tag and the N-terminus of either *C. glutamicum* ATCC13032 *odhA* (Uniprot accession no. Q8NRC3, residues 1-1221) or *odhI* (Uniprot accession no. Q8NQJ3, residues 1-143). The pET-28a-TEV/$OdhA_{\Delta 97}$ construct (coding for OdhA residues 98-1221) was also generated by Genscript from pET-28a-TEV/OdhA.

Protein purification. Full-length *Ms*KGD was overexpressed in *E. coli* BL21(DE3)pLysS and purified as previously described [18]. Both OdhA expression constructs (pET-28a-TEV/OdhA and pET-28a-TEV/$OdhA_{\Delta 97}$) were introduced into *E. coli* BL21(DE3), and protein expression achieved following the same autoinduction scheme. [37] Recombinant proteins were also purified following the same protocol. After an overnight incubation at 30 °C in 2YT-based autoinduction medium containing 50 µg/ml kanamycin, cells were harvested and frozen at -80 °C. Cell pellets were resuspended in 50 ml lysis buffer (25 mM Tris pH 8.5, 300 mM NaCl, 25 mM imidazole, supplemented with benzonase and EDTA-free protease inhibitor cocktails (Roche)) at 4 °C, and lysed by a CF2 cell disruptor (Constant Systems Ltd., Daventry, UK). The lysate was centrifuged for one hour at 13,000 ×*g* at 4 °C. The clear supernatant was loaded onto a Ni-NTA affinity chromatography column (1 ml HisTrap FF crude, Cytiva), and his-tagged proteins were eluted with a linear gradient of buffer B (25 mM Tris pH 8.5, 300 mM NaCl, 400 mM imidazole). The eluted fractions containing the protein of interest were pooled and TEV protease was added when appropriate (1:30 w/w ratio). The sample was then dialyzed overnight at 4 °C against 20 mM Hepes pH 7.5, 500 mM NaCl, 1 mM DTT using 'SnakeSkin' dialysis tubing with a 7 kDa molecular weight cut-off (ThermoFisher). His_6-tagged cleavage products as well as TEV protease were removed with Ni-NTA agarose resin (Qiagen) on gravity flow disposable plastic columns. The sample was then concentrated and loaded onto a Sephacryl S-400 HR 16/60 size exclusion (SEC) column (Cytiva) pre-equilibrated in 20 mM Hepes pH 7.5, 500 mM NaCl (20 mM Hepes pH 7.5,

300 mM NaCl for OdhA$_{\Delta 97}$). Fractions corresponding to the OdhA peak were checked on SDS-PAGE, pooled and concentrated. The resulting sample was either used directly for cryo-EM grid preparation, or flash-frozen in small aliquots in liquid nitrogen and stored at −80 °C. The pET-28a-TEV/*Ms*KGDΔ96 construct was also introduced in *E. coli* BL21(DE3), but protein expression was achieved in LB media, at 30 °C, by induction with 0.75 mM IPTG for 3 h 20 min. Purification followed the procedure above, except for the dialysis and size-exclusion buffer, which was 25 mM Tris-HCl pH 7.6, 150 mM NaCl, 1 mM DTT.

Likewise, OdhI was overexpressed by autoinduction in the same 2YT-based medium as OdhA, but overnight culture at 14 °C. The purification also followed the protocol above, but size-exclusion chromatography was performed on a HiLoad Superdex 75 16/60 column run in 25 mM Tris-HCl pH 8.5, 150 mM NaCl. *M. smegmatis* GarA was expressed and purified as described [22].

Crystallization. Initial crystallization screenings were performed at 18 °C by vapour diffusion in 96-well plates, according to established protocols at the Crystallography Core Facility of the Institut Pasteur [38]. Crystals of the OdhA$_{\Delta 97}$-CoASH complex were obtained from a 26 mg/ml OdhA$_{\Delta 97}$ solution, supplemented with 5 mM CoASH and crystallized in 0.1 M Hepes-NaOH pH 7.5, 5% (w/v) PEG 4000, 30% (v/v) methylpentanediol (MPD) by the sitting drop method; for the *Ms*KGD-GarA complex, crystals were obtained from a 10 mg/ml *Ms*KGD solution supplemented with 2 mM ThDP, 5 mM $MgCl_2$ and *M. smegmatis* GarA (1:1 molar ratio), and crystallized, through the hanging drop method, in 0.1 M bicine pH 8.0, 30% (v/v) PEG550MME, 0.2 M NaCl.

X-ray diffraction data collection and structure solution. Diffraction datasets were acquired either on the beamline ID30A-3 at the ESRF synchrotron (Grenoble, France), or on the beamline Proxima-1 at the SOLEIL synchrotron (Saint-Aubin, France). Data integration and scaling were performed with *autoPROC* [39], applying anisotropic scaling via *STARANISO*. Structures were solved by molecular replacement through the program *PHASER* [40], using the previously released coordinates of the *Ms*KGD$_{\Delta 115}$ homodimer (PDB 2XT6; [18]) as the search model for both datasets (OdhA$_{\Delta 97}$-CoA and

449 *Ms*KGD:GarA). *M. smegmatis* GarA coordinates were retrieved from the previously published
450 *Ms*KGD$_{\Delta 360}$:GarA complex (pdb 6I2Q; [22]). Manual model rebuilding and ligand placement in electron
451 density maps was entirely performed with *COOT* [41]. Refinement was carried out with *BUSTER*,
452 applying local structure similarity restraints for non-crystallography symmetry (NCS) [42] where
453 appropriate, and a Translation-Libration-Screw (TLS) model. Chemical dictionaries for ligands were
454 generated with the Grade server (http://grade.globalphasing.org). Validation of models was performed
455 with *MOLPROBITY* [43] and the validation tools in *PHENIX* [44]. Data collection, refinement and model
456 statistics are indicated in **Table 1**.
457
458 **Negative staining EM**. 5 µl of purified OdhA sample, at concentrations of either 0.05 mg/ml or 0.01
459 mg/ml, were applied over 400-mesh copper carbon coated grids (Electron Microscopy Sciences) that
460 were previously glow discharged at 2 mA for 20 s. Grids were washed twice in 10 µl water for 40 s,
461 then stained in a 2% uranyl acetate solution (twice for 40 s). Grids were then blotted using a Whatman
462 1 filter paper and air dried for 5 min. Micrographs were acquired on a Tecnai T12 transmission electron
463 microscope (ThermoScientific), operating at 120 kV, at magnification rates comprised between 30,000x
464 and 180,000x.
465
466 **Cryo-EM sample preparation and data collection.** OdhA samples were vitrified at a concentration
467 of 12.0 mg/ml (protein without ligands, incubated with CoASH or succinyl-CoA), or 8.0 mg/ml for the
468 OdhA-SP complex. The OdhA:OdhI complex was prepared by incubating a mixture of the two proteins
469 at molar ratio 1:10, which was then subjected to size-exclusion chromatography on a Superose 6
470 increase 5/150 GL column (Cityva), run in 20 mM Hepes pH 7.5, 500 mM NaCl. UltrAuFoil R1.2/1.3
471 300 mesh gold grids (Quantifoil) were used for OdhA alone, OdhA-CoASH or OdhA-succinyl-CoA,
472 while OdhA-SP and OdhA:OdhI were vitrified on Lacey carbon 200 mesh grids (Electron Microscopy
473 Sciences). Grids were glow discharged for 25 s at 50 W (UltrAuFoil R1.2/1.3) or 10 s at 5 W (Lacey)
474 with a Solarus II plasma cleaner (Gatan). Vitrification was carried out using a Vitrobot Mark IV
475 (ThermoScientific), applying 3 µl of protein sample to the grid surface at a temperature of 4°C and

476 humidity level of 100%. Grids were then blotted (during 4 s at blot force 0 for Lacey grids, blot force 2
477 for UltrAuFoil R1.2/1.3 grids) and plunge-frozen into liquid ethane. Data from all samples but OdhA-
478 succinyl-CoA were collected at the Nanoimaging Core facility in Institut Pasteur on a Titan Krios
479 electron microscope (ThermoScientific), operated at 300 kV and equipped with a K3 direct electron
480 detector (Gatan) operating in counted mode. The OdhA-succinyl-CoA dataset was instead collected on
481 a Titan Krios microscope located at the ESRF (Grenoble, France), also running at 300 kV and equipped
482 by a K3 detector operating in the counted super-resolution mode. The software EPU 2
483 (ThermoScientific) was used to pilot data collection in all cases. A summary of data collection and
484 model refinement parameters is reported in **Table 2**. The OdhA-succinyl-CoA raw data will be available
485 under the DOI 10.15151/ESRF-ES-514136397.
486
487 **Single particle analysis of cryo-EM data.** All single particle cryo-EM datasets were processed through
488 cryoSPARC version 3.2 [45]. Motion correction was performed using full-frame motion correction and
489 CTF estimation were performed using patch CTF estimation. Using the curate exposure feature, 12666
490 out of 13348 for OdhA alone, 7996 out of 12202 for OdhA-CoASH, 8796 out of 11827 for OdhA-
491 succinyl-CoA, 15025 out of 16647 for OdhA-SP, and 14842 out of 19443 for OdhA-OdhI complex
492 were selected for further analysis. A first round of 'blob particle picking' was performed, and after 2D
493 classification, the most populated classes were selected for template-based particle picking against a
494 dataset containing the selected micrographs. Particles were extracted applying a box size of 384 Å,
495 except for the OdhA-SP sample for which the box size was set at 448 Å. The extracted particles were
496 cleaned using the 'inspect pick' function of Cryosparc and several rounds of 2D classification with
497 selection of higher resolution classes were applied, selecting classes corresponding to a complete,
498 hexamer shape of OdhA in different orientations. The selected particles were used, after local motion
499 correction, to build an *ab-initio* model and non-uniform 3D refinement applying D3 symmetry, while
500 optimizing per-particle defocus and per-group CTF parameters. For all datasets, local refinement was
501 performed with a soft mask covering the OdhA E1o domain dimer. A composite map including the
502 three OdhA E1o dimers was generated by the 'combine focused maps' tool in PHENIX (v. 1.20-4459-
503 000) [44].

Single particle EM model building and refinement. OdhA coordinates obtained from X-ray crystallography were fitted into the corresponding cryo-EM density maps using UCSF Chimera (v1.13.1) [46]. For the OdhA-OdhI complex, *C. glutamicum* OdhI coordinates were retrieved from the available crystal structure (pdb 4QCJ; [47]). Following a first round of rigid-body fitting of the E2o and E1o OdhA domains, and OdhI were appropriate, the models were improved by iterative rounds of restrained real-space refinement in *PHENIX*, and alternating rounds of model building with manual adjustment in *COOT* and further model refinement through the Servalcat pipeline [48] in the CCP-EM suite [49]. Model validations were performed using the specific tools in the *PHENIX* and CCP-EM suites. Figures were prepared using UCSF ChimeraX v.1.3 [50], and PyMOL v. 2.5.4 [51].

Surface plasmon resonance binding assay. Experiments were performed using a Biacore T200 instrument (Cytiva) and NTA sensorchips equilibrated at 25°C in OdhA storage buffer (20 mM Hepes pH 7.5, 500 mM NaCl), complemented with 100 µM EDTA and 0.2 mg/ml BSA. Two flow cells of the chip were first activated by running a 1 mM $NiCl_2$ solution for 2 min at 5 µl/min, and loaded with OdhA-His_6 (200 µg/ml) for 10 min at 5 µl/min, reaching densities of 8800 – 10000 resonance units (RU, ≈ pg/mm^2). 5 concentrations of SP were then injected sequentially in single cycle kinetics mode at 30 µl/min for 2 min each, followed by a 2 min buffer wash to monitor the dissociation of the OdhA-SP transient complex. The sensorchip was finally fully regenerated by injecting 0.5 M EDTA, 0.1% SDS twice for 2 min at 5 µl/min, allowing it to be reused for a new experimental cycle. Sensorgrams were processed using the BiaEvaluation software. The concentration-dependence of steady-state SPR signals (Req) was analysed using the following equation: Req = Rmax * C / Kd + C, where C is the SP concentration and Rmax the fitted maximal SPR signal at infinite SP concentration.

Analytical Ultracentrifugation. Sedimentation velocity (SV) analytical ultracentrifugation assays were performed using a Beckman Coulter ProteomeLab XL-I analytical ultracentrifuge equipped with UV-Vis absorbance and Raleigh interference detection systems, using an 8-hole Beckman An-50 Ti rotor at 20°C. Experiments were performed at 30,000 rpm. Seven concentrations (from 4 mg/ml to

0.0625 mg/ml, serial two-fold dilutions) were prepared for this experiment in the OdhA buffer (20 mM Hepes pH 7.5, 500 mM NaCl) and loaded into analytical ultracentrifugation cells. During the run, SV was followed by measuring absorbance at 280 nm for sample with concentration from 4 mg/ml to 0.25 mg/ml and at 225 nm for sample with concentration at 0.125 mg/ml and 0.0625 mg/ml. The software SEDFIT v. 15.01 [52] was used to calculate the sedimentation coefficient distribution C(s), then corrected to standard conditions to get the final standard values. Coefficients were plotted as a function of the different concentrations and an extrapolation to zero concentration was made to obtain the standard value for the main oligomer. From these values, molecular mass and friction ratio were obtained.

Protein sequence analyses. Sequence analyses were carried out on a database representing all Actinobacteria diversity present at the National Center for Biotechnology (NCBI) as of February 2021, containing 133 taxa (five species per class). To identify OdhA homologs, the jackhmmer tool from the HMMER package (v3.3.2) [53] was employed, using the GenBank [54] sequence BAB98522.1 as the query. The hits were aligned with mafft (v7.475) [55] accurate option linsi. The MSA was manually curated, removing sequences that did not align. A sequence logo of OdhA was created based on the MSA through the online tool WebLogo3 [56]. The secondary structure of protein OdhA was mapped on the MSA using the online tool ESPript [57].

References

1. Perham, R. N. Swinging arms and swinging domains in multifunctional enzymes: catalytic machines for multistep reactions. *Annu. Rev. Biochem.* 69, 961–1004 (2000).

2. Rajashankar, K. R. *et al.* Crystal structure and functional analysis of lipoamide dehydrogenase from *Mycobacterium tuberculosis*. *J. Biol. Chem.* 280, 33977–33983 (2005).

3. Byron, O. & Lindsay, J. G. The Pyruvate Dehydrogenase Complex and Related Assemblies in Health and Disease. in *Macromolecular Protein Complexes* vol. 83 523–550 (Macromolecular Protein Complexes, 2017).

4. DeRosier, D. J., Oliver, R. M. & Reed, L. J. Crystallization and preliminary structural analysis of dihydrolipoyl transsuccinylase, the core of the 2-oxoglutarate dehydrogenase complex. *Proc. Natl. Acad. Sci. USA* 68, 1135–1137 (1971).

5. Reed, L. J., Fernandez-Moran, H., Koike, M. & Willms, C. R. Electron Microscopic And Biochemical Studies Of Pyruvate Dehydrogenase Complex Of *Escherichia coli*. *Science* 145, 930–932 (1964).

6. Mattevi, A. *et al.* Atomic structure of the cubic core of the pyruvate dehydrogenase multienzyme complex. *Science* 255, 1544–1550 (1992).

7. Knapp, J. E. *et al.* Crystal structure of the truncated cubic core component of the *Escherichia coli* 2-oxoglutarate dehydrogenase multienzyme complex. *J. Mol. Biol.* 280, (1998).

8. Izard, T. *et al.* Principles of quasi-equivalence and Euclidean geometry govern the assembly of cubic and dodecahedral cores of pyruvate dehydrogenase complexes. *Proc. Natl. Acad. Sci. USA* 96, 1240–1245 (1999).

9. Kato, M. *et al.* A synchronized substrate-gating mechanism revealed by cubic-core structure of the bovine branched-chain alpha-ketoacid dehydrogenase complex. *EMBO J.* 25, 5983–5994 (2006).

10. Milne, J. L. S. *et al.* Molecular structure of a 9-MDa icosahedral pyruvate dehydrogenase subcomplex containing the E2 and E3 enzymes using cryoelectron microscopy. *J. Biol. Chem.* 281, 4364–4370 (2006).

11. Vijayakrishnan, S. *et al.* Solution structure and characterisation of the human pyruvate dehydrogenase complex core assembly. *J. Mol. Biol.* 399, 71–93 (2010).

12. Škerlová, J., Berndtsson, J., Nolte, H., Ott, M. & Stenmark, P. Structure of the native pyruvate dehydrogenase complex reveals the mechanism of substrate insertion. *Nat. Commun.* 12, 5277 (2021).

13. Kyrilis, F. L. *et al.* Integrative structure of a 10-megadalton eukaryotic pyruvate dehydrogenase complex from native cell extracts. *Cell Reports* 34, 108727 (2021).

14. Forsberg, B. O., Aibara, S., Howard, R. J., Mortezaei, N. & Lindahl, E. Arrangement and symmetry of the fungal E3BP-containing core of the pyruvate dehydrogenase complex. *Nat. Commun.* 1–10 (2020) .

15. Usuda, Y. *et al.* Molecular cloning of the *Corynebacterium glutamicum* ("Brevibacterium lactofermentum" AJ12036) odhA gene encoding a novel type of 2-oxoglutarate dehydrogenase. *Microbiology* 142, 3347–3354 (1996).

588 16. Hoffelder, M., Raasch, K., Ooyen, J. van & Eggeling, L. The E2 domain of OdhA of
589 *Corynebacterium glutamicum* has succinyltransferase activity dependent on lipoyl residues of the
590 acetyltransferase AceF. *J. Bacteriol.* 192, 5203–5211 (2010).

591 17. Niebisch, A., Kabus, A., Schultz, C., Weil, B. & Bott, M. Corynebacterial protein kinase G controls
592 2-oxoglutarate dehydrogenase activity via the phosphorylation status of the OdhI protein. *J. Biol. Chem.*
593 281, 12300–7 (2006).

594 18. Wagner, T., Bellinzoni, M., Wehenkel, A., O'Hare, H. M. & Alzari, P. M. Functional plasticity and
595 allosteric regulation of α-ketoglutarate decarboxylase in central mycobacterial metabolism. *Chem. Bio.l*
596 18, 1011–1020 (2011).

597 19. Tian, J. *et al. Mycobacterium tuberculosis* appears to lack alpha-ketoglutarate dehydrogenase and
598 encodes pyruvate dehydrogenase in widely separated genes. *Mol. Microbiol.* 57, 859–868 (2005).

599 20. Bruch, E. M. *et al.* Actinobacteria challenge the paradigm: A unique protein architecture for a well-
600 known, central metabolic complex. *Proc Natl. Acad. Sci. USA* 118, e2112107118 (2021).

601 21. Mattevi, A., Obmolova, G., Kalk, K. H., Teplyakov, A. & Hol, W. G. J. Crystallographic Analysis
602 of Substrate Binding and Catalysis in Dihydrolipoyl Transacetylase (E2p). *Biochemistry* 32, 3887–3901
603 (1993).

604 22. Wagner, T. *et al.* Structural insights into the functional versatility of an FHA domain protein in
605 mycobacterial signaling. *Sci Signal.* 12, eaav9504 (2019).

606 23. Zhou, J. *et al.* A multipronged approach unravels unprecedented protein-protein interactions in the
607 human 2-oxoglutarate dehydrogenase multienzyme complex. *J. Biol. Chem.* 293, 19213–19227 (2018).

608 24. Wagner, T., Barilone, N., Alzari, P. M. & Bellinzoni, M. A dual conformation of the post-
609 decarboxylation intermediate is associated with distinct enzyme states in mycobacterial KGD (α-
610 ketoglutarate decarboxylase). *Biochem. J.* 457, 425–434 (2014).

611 25. Wagner, T., Boyko, A., Alzari, P. M., Bunik, V. I. & Bellinzoni, M. Conformational transitions in
612 the active site of mycobacterial 2-oxoglutarate dehydrogenase upon binding phosphonate analogues of
613 2-oxoglutarate: From a Michaelis-like complex to ThDP adducts. *J. Struct. Biol.* 208, 182–190 (2019).

614 26. Chen, J., Noble, A. J., Kang, J. Y. & Darst, S. A. Eliminating effects of particle adsorption to the
615 air/water interface in single-particle cryo-electron microscopy: Bacterial RNA polymerase and
616 CHAPSO. *J Struct Biol. X* 1, 100005 (2019).

617 27. Balakrishnan, A., Jordan, F. & Nathan, C. F. Influence of allosteric regulators on individual steps
618 in the reaction catalyzed by *Mycobacterium tuberculosis* 2-hydroxy-3-oxoadipate synthase. *J. Biol.*
619 *Chem.* 288, 21688–21702 (2013).

620 28. O'Hare, H. M. *et al.* Regulation of glutamate metabolism by protein kinases in mycobacteria. *Mol.*
621 *Microbiol.* 70, 1408–1423 (2008).

622 29. Krawczyk, S. *et al.* The FHA domain of OdhI interacts with the carboxyterminal 2-oxoglutarate
623 dehydrogenase domain of OdhA in *Corynebacterium glutamicum*. *FEBS Lett.* 584, 1463–1468 (2010).

624 30. Sundermeyer, L. *et al.* Characteristics of the GlnH and GlnX Signal Transduction Proteins
625 Controlling PknG-Mediated Phosphorylation of OdhI and 2-Oxoglutarate Dehydrogenase Activity in
626 *Corynebacterium glutamicum*. *Microbiol. Spectr.* e02677-22 (2022) doi:10.1128/spectrum.02677-22.

627 31. Punjani, A. & Fleet, D. J. 3D variability analysis: Resolving continuous flexibility and discrete
628 heterogeneity from single particle cryo-EM. *J. Struct. Biol.* 213, 107702 (2021).

629 32. Tüting, C. *et al.* Cryo-EM snapshots of a native lysate provide structural insights into a metabolon-
630 embedded transacetylase reaction. *Nat. Commun.* 12, 6933 (2021).

631 33. Jiang, J. *et al.* Atomic Structure of the E2 Inner Core of Human Pyruvate Dehydrogenase Complex.
632 *Biochemistry* 57, 2325–2334 (2018).

633 34. Liu, S., Xia, X., Zhen, J., Li, Z. & Zhou, Z. H. Structures and comparison of endogenous 2-
634 oxoglutarate and pyruvate dehydrogenase complexes from bovine kidney. *Cell Discov.* 8, 126 (2022).

635 35. Kinugawa, H. *et al.* In vitroreconstitution and characterization of pyruvate dehydrogenase and 2-
636 oxoglutarate dehydrogenase hybrid complex from *Corynebacterium glutamicum*. *Microbiologyopen* 5,
637 593–14 (2020).

638 36. Mattevi, A. How evolution dismantles and reassembles multienzyme complexes. *Proc National*
639 *Acad Sci USA* 119, e2120286118 (2022).

640 37. Studier, F. W. Protein production by auto-induction in high density shaking cultures. *Protein Expr.*
641 *Purif.* 41, 207–234 (2005).

642 38. Weber, P. *et al.* High-Throughput Crystallization Pipeline at the Crystallography Core Facility of
643 the Institut Pasteur. *Molecules* 24, (2019).

644 39. Vonrhein, C. *et al.* Data processing and analysis with the autoPROC toolbox. *Acta Crystallogr. D*
645 *Biol. Crystallogr.* 67, 293–302 (2011).

646 40. McCoy, A. J. *et al.* Phaser crystallographic software. *J. Appl. Crystallogr.* 40, 658–674 (2007).

647 41. Emsley, P., Lohkamp, B., Scott, W. G. & Cowtan, K. Features and development of Coot. *Acta*
648 *Crystallogr. D Biol. Crystallogr.* 66, 486–501 (2010).

649 42. Smart, O. S. *et al.* Exploiting structure similarity in refinement: automated NCS and target-structure
650 restraints in BUSTER. *Acta Crystallogr. D Biol. Crystallogr.* 68, 368–380 (2012).

651 43. Williams, C. J. *et al.* MolProbity: More and better reference data for improved all-atom structure
652 validation. *Protein Sci.* 27, 293–315 (2018).

653 44. Liebschner, D. *et al.* Macromolecular structure determination using X-rays, neutrons and electrons:
654 recent developments in Phenix. *Acta Crystallogr. D Struct. Biol.* 75, 861–877 (2019).

655 45. Punjani, A., Rubinstein, J. L., Fleet, D. J. & Brubaker, M. A. cryoSPARC: algorithms for rapid
656 unsupervised cryo-EM structure determination. *Nat. Meth.* 14, 290–296 (2017).

657 46. Pettersen, E. F. *et al.* UCSF Chimera—A visualization system for exploratory research and analysis.
658 *J Comput. Chem.* 25, 1605–1612 (2004).

659 47. Raasch, K. *et al.* Interaction of 2-oxoglutarate dehydrogenase OdhA with its inhibitor OdhI in
660 *Corynebacterium glutamicum*: Mutants and a model. *J. Biotechnol.* 191, (2014).

661 48. Yamashita, K., Palmer, C. M., Burnley, T. & Murshudov, G. N. Cryo-EM single-particle structure
662 refinement and map calculation using Servalcat. *Acta Crystallogr. Sect. D Struct. Biology* 77, 1282–
663 1291 (2021).

664 49. Burnley, T., Palmer, C. M. & Winn, M. Recent developments in the CCP-EM software suite. *Acta*
665 *Crystallogr. Sect. D Struct. Biology* 73, 469–477 (2017).

666 50. Pettersen, E. F. *et al.* UCSF ChimeraX: Structure visualization for researchers, educators, and
667 developers. *Protein Sci.* 30, 70–82 (2021).

668 51. Schrödinger, LLC. *The PyMOL Molecular Graphics System*, Version 2.5.4 (2022).

669 52. Schuck, P. Size-Distribution Analysis of Macromolecules by Sedimentation Velocity
670 Ultracentrifugation and Lamm Equation Modeling. *Biophys J* 78, 1606–1619 (2000).

671 53. Johnson, L. S., Eddy, S. R. & Portugaly, E. Hidden Markov model speed heuristic and iterative
672 HMM search procedure. *BMC Bioinformatics* 11, 431 (2010).

673 54. Sayers, E. W. *et al.* GenBank. *Nucleic Acids Res.* 49, gkaa1023- (2020).

674 55. Katoh, K. & Standley, D. M. MAFFT multiple sequence alignment software version 7:
675 Improvements in performance and usability. *Mol. Biol. Evol.* 30, 772–780 (2013).

676 56. Crooks, G. E., Hon, G., Chandonia, J.-M. & Brenner, S. E. WebLogo: A Sequence Logo Generator.
677 *Genome Res.* 14, 1188–1190 (2004).

678 57. Robert, X. & Gouet, P. Deciphering key features in protein structures with the new ENDscript
679 server. *Nucleic Acids Res.* 42, W320-4 (2014).

680

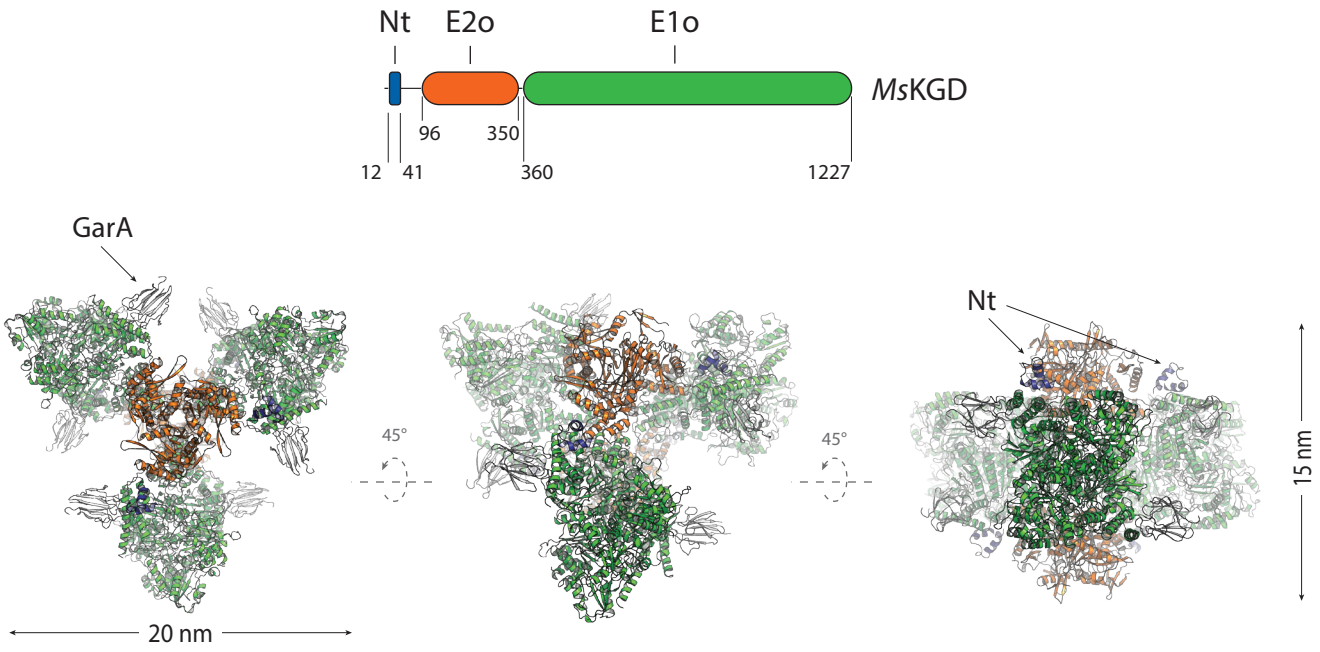

Figure 1. Domain boundaries in *Ms*KGD (Nt: N-terminal helical domain) and cartoon overview of the *Ms*KGD hexamer in complex with GarA (grey).

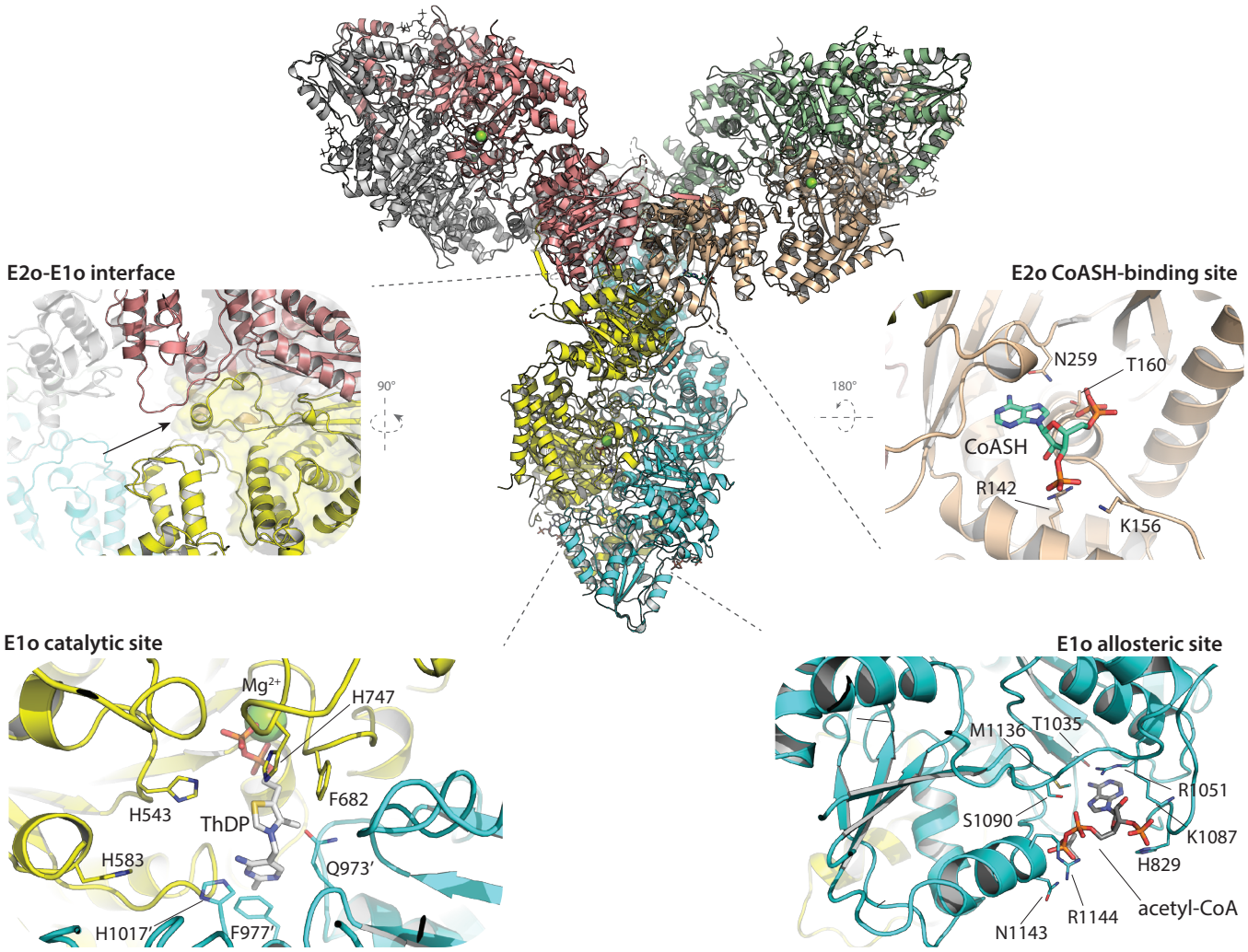

Figure 2. Centre: cartoon overview of the $OdhA_{\Delta 97}$ homohexamer (one colour per chain), with the single protomers related by crystallographic symmetry. Laterally, in anticlockwise sense, detailed views of: E2o-E1o interface, with surface highligthed for the E2o domain (arrow pointing to the short α-helix between residues Glu296-Leu302; see also Suppl. Fig. 4); E1o catalytic site at the protomer interface, the ThDP-Mg^{2+} cofactor at the centre; E1o allosteric acetyl-CoA binding site; E2o CoASH binding site. Indicated in the figure and depicted as sticks are the side chains of either significant residues interacting with cofactor or ligands through hydrogen bonds, salt bridges or van der Waals interactions, or, in the case of the E1o catalytic site, with a predicted role in catalysis (namaly His543, His583, His747 and His1017, as reported for *Ms*KGD [18]).

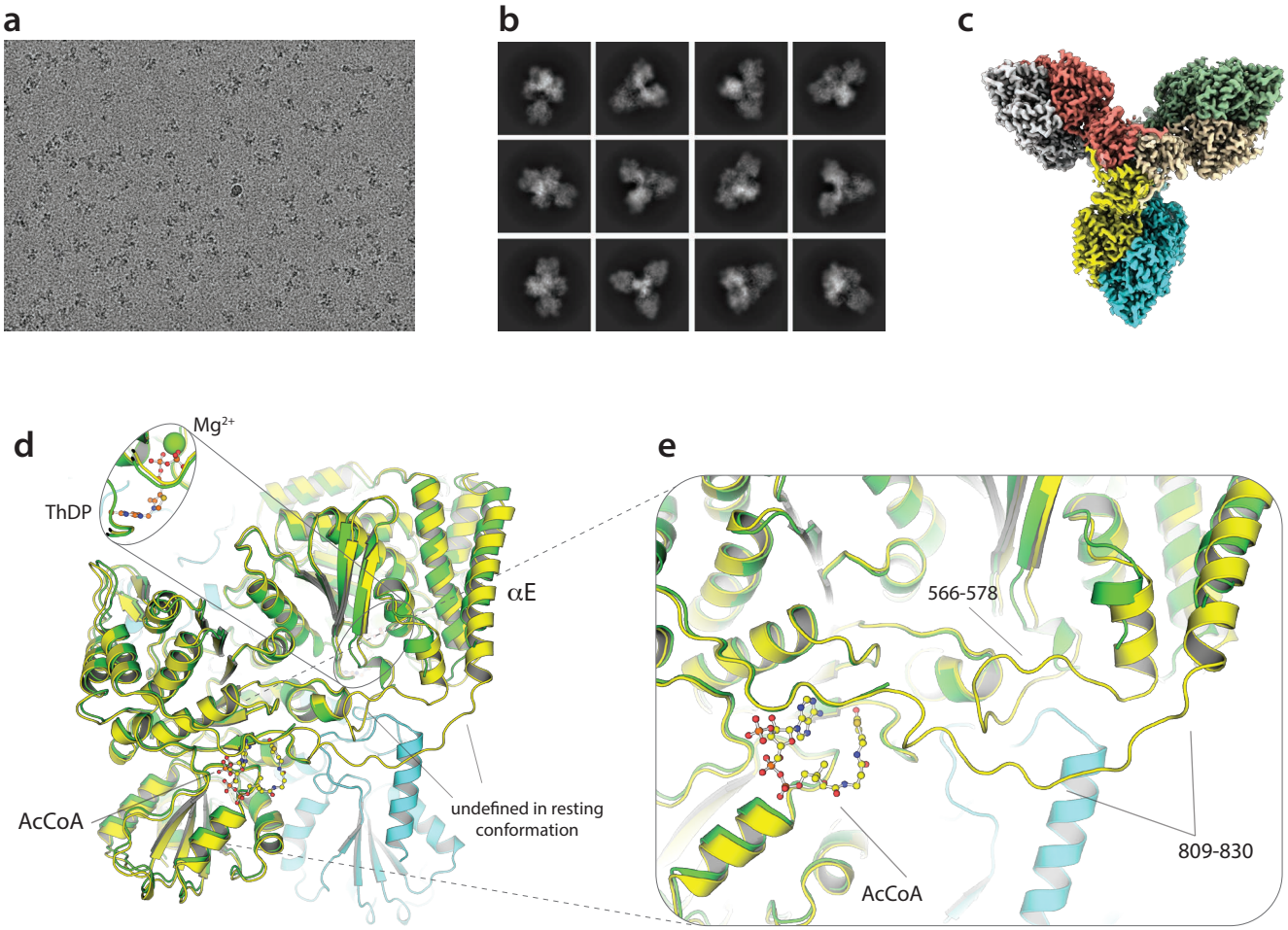

Figure 3. (**a**) Representative micrograph of an OdhA sample vitrified on an UltraAuFoil grid (Quantifoil). (**b**) Representative 2D classes from the same dataset as in (a). (**c**) Overall representation of the OdhA map at 2.2 Å resolution, showing the OdhA homohexamer (one colour per chain). (**d**) Superimposition, focused on the E1o domain, of the OdhA$_{\Delta 97}$ model (green) to the OdhA model determined by single particle cryo-EM in the absence of added ligands (yellow/light blue). Loops that could not be traced in OdhA$_{\Delta 97}$ are indicated. Also to be noted the different position of the αE external helix (see also Suppl. Fig. 12). (**e**) Zoomed view on the region most concerned by the conformational change, from the resting conformation (observed for the OdhA$_{\Delta 97}$ crystal structure) to the active conformation observed by cryo-EM. Loops that become well defined in the active conformation are indicated, as well as the acetyl-CoA molecule observed in the allosteric E1o pocket in the OdhA model obtained by cryo-EM. An acetyl-CoA molecule bound in the same pocket was observed in all the OdhA complexes solved by single particle cryo-EM, with the exception of the OdhA-OdhI complex. The OdhA$_{\Delta 97}$model also presents a CoA esther (presumably acetyl-CoA) bound in the same pocket, although the lack of supporting electron density hindered tracing of the whole pantothenate chain (**Fig. 2**).

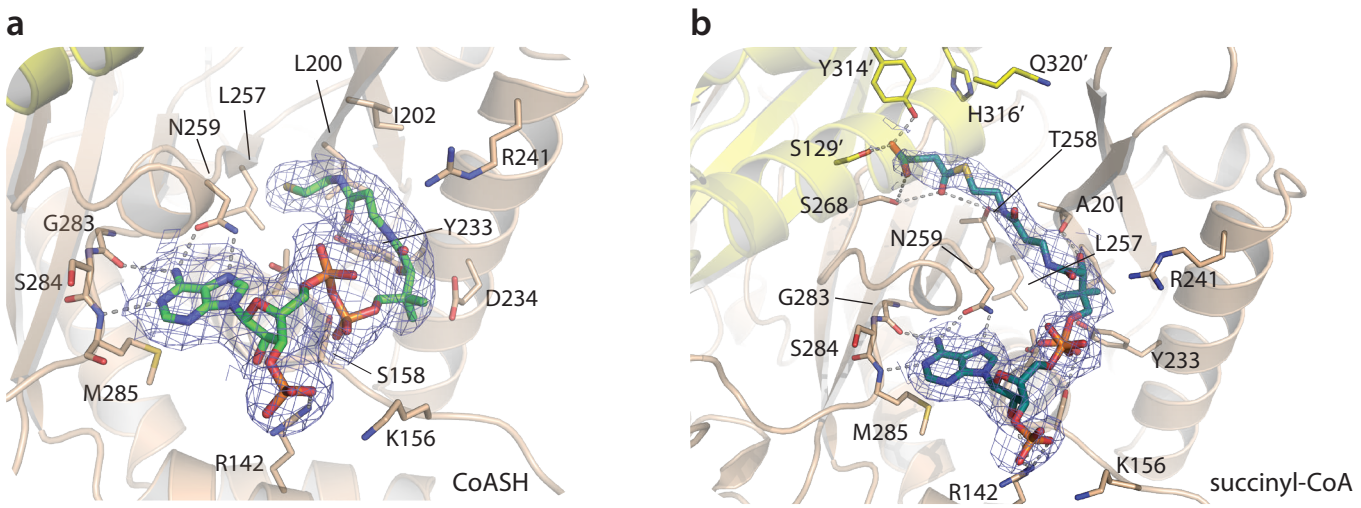

Figure 4. Cartoon representation of CoASH (**a**) vs. succinyl-CoA (**b**) binding in the OdhA E2o active site, as determined by high-resolution single particle cryo-EM. To note, the terminal sulphydryl group of CoASH does not reach the catalytic centre (identifiable by the His316/Gln320 diad), but is accommodated in a mostly hydrophobic pocket defined by Leu200, Ile202, and Leu257, with the hydroxyl group of Tyr233 acting as an hydrogen bond donor to the terminal carbonyl oxygen of CoASH. This binding orientation, although not identical, corresponds to the 'OUT' conformation originally observed in the ternary complex of *A. vinelandii* E2p with CoASH and free lipoamide (PDB 1EAB; Suppl. Fig. 14). Blue meshes corresponds to the EM map for the ligands, contoured at the 3.5σ level.

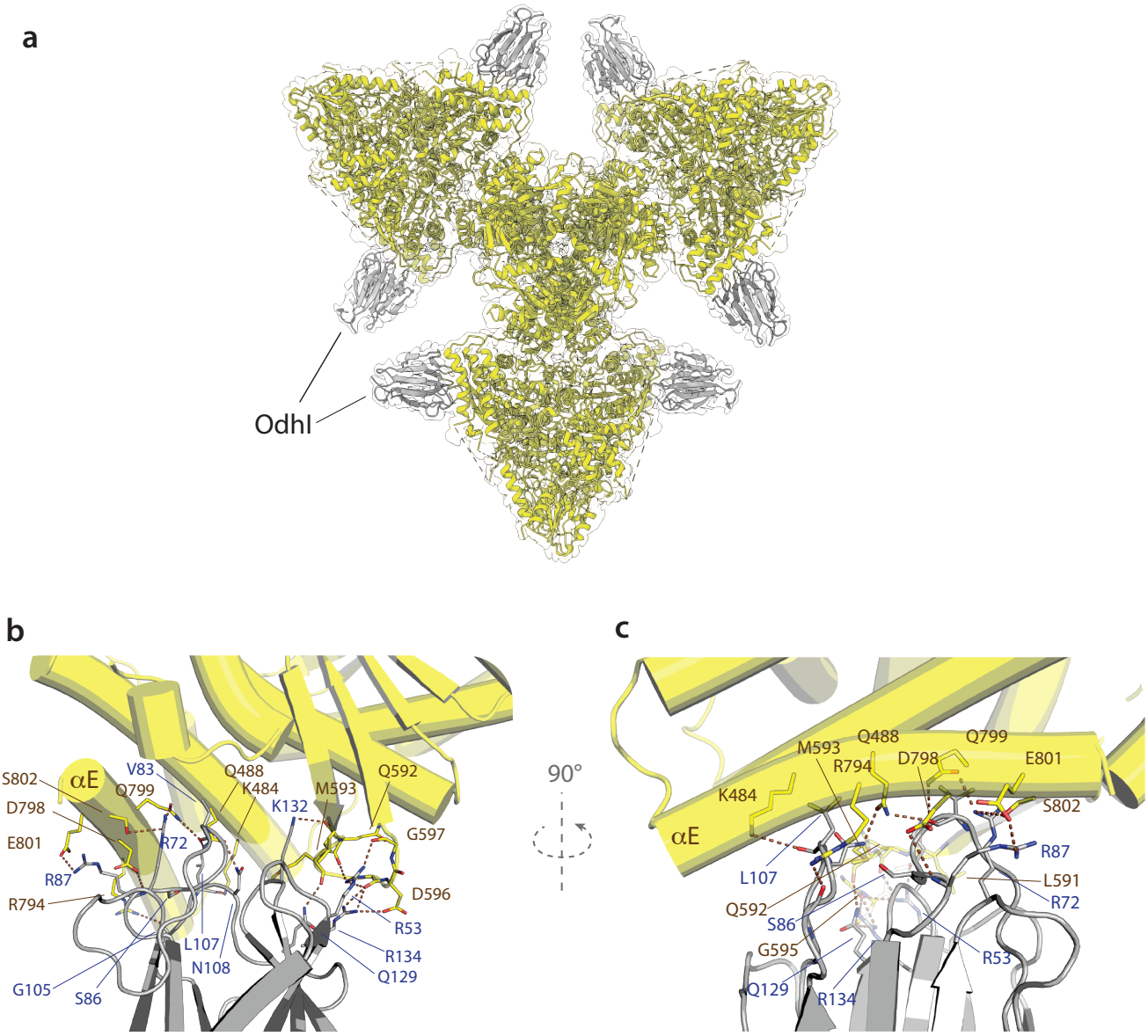

Figure 5. (**a**) Visualization of the OdhA-OdhI complex fit in the corresponding single particle EM map at 2.3 Å resolution. (**b**) Detailed view of the interactions between OdhA (yellow) and OdhI FHA domain (grey), with the involved residues depicted as sticks. Dashed lines indicate hydrogen bonds and salt bridges. OdhA helices are depicted as cylinders. (**c**) Rotated view of the OdhA-OdhI interactions. αE refers to the OdhA α-helix Ser785-Asn805, following the original *Ms*KGD nomenclature.

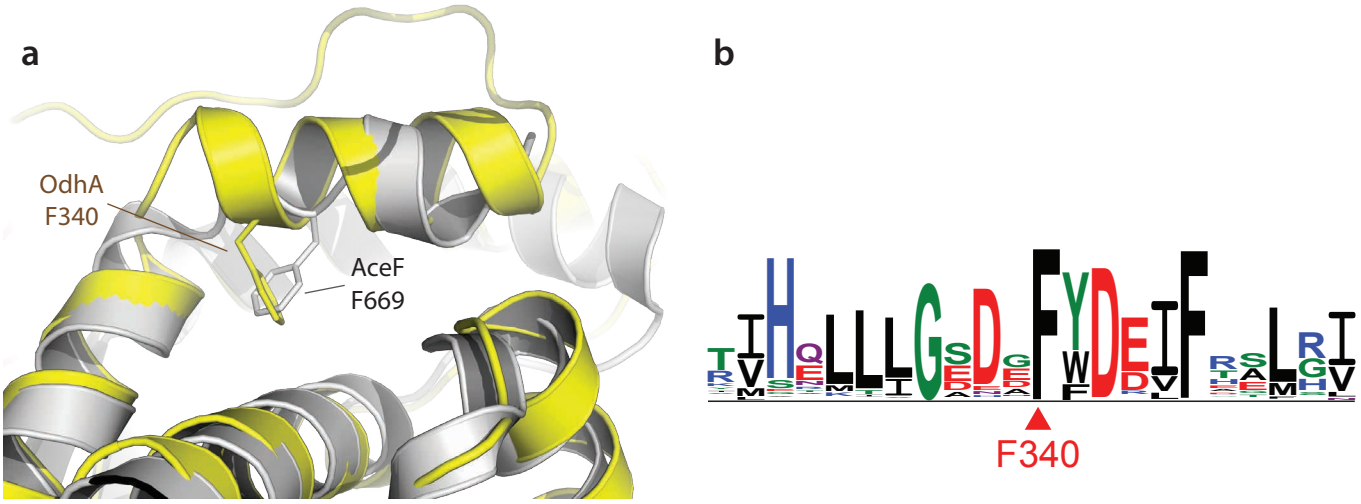

Figure 6. (**a**) Superimposition of the E2o domain of OdhA (yellow) to the catalytic domain of *C. glutamicum* E2p (AceF; grey, PDB 6ZZI [20]). Focus is on the amphipatic helix that marks the C-terminal boundary of the OdhA E2o domain, which shows the same relative position as the C-terminal helix in AceF. To note the presence of a structurally conserved phenylalanine residue (indicated) that, in both proteins, contributes to maintain the helix relative orientation through intramolecular interactions. Such orientation was shown to be key to the loss of high-order oligomerisation in actinobacterial E2p enzymes. (**b**) Sequence logo derived from a multiple sequence alignement of OdhA orthologues from representative members of the Actinobacteria phylum (see Suppl. Fig. 16). The logo is here limited to the OdhA residues surrounding the conserved Phe340.

Table 1. Crystallographic data collection and refinement statistics.

Dataset	***Ms*KGD-GarA**	**OdhA$_{\Delta 97}$**
Synchrotron beamline	SOLEIL Proxima 1	ESRF ID30A-3
Wavelength (Å)	0.9763	0.9677
Space group	P 6_5	H 3 2
Unit cell parameters		
a, *b*, *c* (Å)	325.75, 325.75, 396.94	150.99, 150.99, 314.34
α, β, γ (°)	90.00, 90.00, 120.00	90.00, 90.00, 120.00
Resolution (Å)	282.11 – 4.56 (4.78 – 4.56)	100.52 – 2.46 (2.70 – 2.46)
R_{pim} [a]	0.076 (0.583)	0.047 (0.466)
$I/\sigma(I)$	8.1 (1.5)	15.5 (1.6)
Completeness (%)	94.6 (52.9)	94.4 (63.8)
CC(1/2)	0.998 (0.701)	0.998 (0.658)
Multiplicity	11.5 (11.8)	10.4 (8.5)
Refinement		
Resolution (Å)	4.56	2.46
No. reflections	121081	38238
R_{work}/ R_{free} (%) [b]	19.8 / 22.9	20.3 / 25.1
No. atoms		
Protein	56835	8366
Ligands/ions	170	110
Solvent	-	362
Average B-factors		
Protein	236.2	59.0
Ligand/ions	223.0	76.7
Solvent	-	48.5
R.m.s deviations		
Bond lengths (Å)	0.006	0.007
Bond angles (°)	0.73	0.86

Resolution limits were determined by applying an anisotropic cut-off via STARANISO, part of the autoPROC data processing software [39]; values in parentheses refer to the highest resolution shell.

[a]$R_{pim} = \Sigma_{hkl}[1/(N-1)]^{1/2}\Sigma_i|I_i(hkl) - \langle I\rangle(hkl)|/\Sigma_{hkl}\,\Sigma_i\, I_i(hkl)$, where N is the multiplicity, I_i is the intensity of reflection i and $\langle I\rangle(hkl)$ is the mean intensity of all symmetry-related reflections.

[b]$R_{work} = \Sigma||F_o| - |F_c||/\Sigma|F_o|$, where F_o and F_c are the observed and calculated structure factor amplitudes. Five percent of the reflections were reserved for the calculation of R_{free}.

Table 2. Cryo-EM data collection, refinement and validation statistics.

Dataset	OdhA	OdhA-CoASH	OdhA-succinyl-CoA	OdhA-SP	OdhA-OdhI
Data collection and processing					
Grid type	UltrAuFoil300 mesh R1.2/1.3	UltrAuFoil300 mesh R1.2/1.3	UltrAuFoil300 mesh R1.2/1.3	Lacey 200mesh	Lacey 200mesh
Plunge freezer	Vitrobot	Vitrobot	Vitrobot	Vitrobot	Vitrobot
Microscope	Krios	Krios	Krios	Krios	Krios
Magnification	105000	105000	105000	105000	105000
Voltage (kV)	300	300	300	300	300
Energy filter(eV)	20	20	20	20	20
Camera	K3	K3	K3	K3	K3
Detector mode	counted	counted	super-resolution	counted	counted
Electron exposure (e–/Å^2)	40	40	48	40	40
Defocus range (μm)	-0.8 to -2.0	-0.8 to -2.0	-0.8 to -2.0	-0.8 to -2.2	-0.8 to -2.2
Pixel size (Å)	0.86	0.86	0.84	0.86	0.86
Micrographs	13348	12202	11827	16647	19443
No. of fractions	40	40	50	60	40
Symmetry imposed	D3	D3	D3	D3	D3
Initial particle images (no.)	6571029	3392043	3827956	2599031	3177955
Final particle images (no.)	1474608	1849406	1074837	646352	958690
Map resolution (Å)#	2.17	2.17	2.07	2.26	2.29
FSC threshold	0.143	0.143	0.143	0.143	0.143
Map resolution range (Å)	1.9-4.4	1.9-4.5	1.9-4.7	2.0-4.6	2.0-6.0
Refinement					
Model resolution (Å)*	2.3	2.2	2.2	2.3	2.3
FSC threshold	0.5	0.5	0.5	0.5	0.5
Map sharpening *B* factor (Å^2)	-84.4	-88.5	-74.2	-87.3	-93.3
Model composition					
No. Atoms (non-H)	52590	52878	52896	52656	55346
Protein residues	6714	6714	6714	6714	7110
Ligands	18	24	24	18	12
Average *B* factors (Å^2)					
Protein	38.53	36.31	82.65	43.36	47.22
Ligands	49.31	49.98	99.56	54.67	123.89
R.m.s. deviations					
Bond lengths (Å)	0.013	0.013	0.003	0.013	0.013
Bond angles (°)	1.787	1.734	0.498	1.736	1.823
Validation*					
MolProbity score	0.88	0.92	1.10	0.95	0.90
Clashscore	1.34	1.69	3.08	1.88	0.66
Poor rotamers (%)	0.31	0.33	0.18	0.34	0.21
Ramachandran plot*					
Favored (%)	97.94	98.12	98.29	98.34	96.87
Allowed (%)	2.06	1.88	1.71	1.66	3.13
Outliers (%)	0	0	0	0	0

Resolution estimates from cryoSPARC (version v3.2.0) [45]

* Values from the EM comprehensive validation tools in *PHENIX* (version 1.20-4459-000) [44]